Sparse and Low-Rank Constrained Tensor Factorization for Hyperspectral Image Unmixing

Pan Zheng, Hongjun Su, *Senior Member, IEEE*, and Qian Du, *Fellow, IEEE*

***Abstract*—Third-order tensors have been widely used in hyperspectral remote sensing because of their ability to maintain the 3-D structure of hyperspectral images. In recent years, hyperspectral unmixing algorithms based on tensor factorization have emerged, but these decomposition processes may be inconsistent with physical mechanism of unmixing. To solve this problem, this article proposes a sparse and low-rank constrained tensor factorization unmixing algorithm based on a matrix-vector nonnegative tensor factorization (MV-NTF) framework. Considering the fact that each component tensor obtained by the image decomposition contains only one endmember and the corresponding abundance matrix has sparse property, a sparse constraint is imposed to ensure the accuracy of abundance maps. Since abundance maps also have low-rank attribute, in order to avoid the strict low-rank constraint in the original MV-NTF framework, a low-rank tensor regularization is introduced to flexibly express the low-rank characteristics of the abundance tensors, making the resulting abundance maps more in line with the actual scene. Then, the optimization problem is solved by using the alternating direction method of multipliers. In experiments, simulated datasets are adopted to demonstrate the effectiveness of the sparse and low-rank constraints of the proposed algorithm, and real datasets from different sensors and different scenarios are used to verify its applicability.**

***Index Terms*—Hyperspectral remote sensing, low-rank, sparse, tensor factorization, unmixing.**

I. Introduction

HYPERSPECTRAL remote sensing technology can effectively distinguish objects that cannot be detected in the traditional multispectral remote sensing technology, making the application of remote sensing technology more refined [1]. A hyperspectral sensor can not only use the imager for ground imaging, but also obtain rich spectral information [2]–[4]. However, due to the limitation of spatial resolution and the homogeneous mixture of distinct materials, pixels in hyperspectral images are often mixed. In order to enhance the accuracy of application, hyperspectral unmixing is widely used. The common unmixing algorithms mainly include endmembers extraction, and then abundance estimation. The performance of endmember extraction greatly affects the accuracy of abundance extraction. For this problem, unsupervised methods of obtaining both endmembers and abundance matrices have become the focus of research. In recent years, many related algorithms have been developed [5]–[9].

One of the most popular algorithms is sparse unmixing by variable splitting and augmented Lagrangian (SUnSAL) in [10], which can estimate abundances without extracting endmembers. The core idea of SUnSAL is to find a few pure spectral vectors that can characterize the image from a prior spectral library as endmembers, and use these endmembers to find the corresponding abundance matrix. In general, the number of endmembers in a spectral library is significantly large, so the abundance matrix has a sparse feature. Based on this method, spatial and spectral information are applied to improve the accuracy of unmixing, SUnSAL-TV considers the spatial neighborhood information and introduces a TV term with SUnSAL [11], [12], which improves the accuracy of hyperspectral unmixing, but lacks effective constraints on abundance coefficients. CLSUnSAL uses a global regularization term, but it does not consider the influence to the row sparseness, due to difference of ground objects in each pixel [13]. Cluster-CLSUnSAL takes into account the differences in endmembers, but it is too time-consuming [14]. These sparse unmixing algorithms improve the accuracy of unmixing to a certain extent [15]. Alternating direction method of multipliers (ADMMs) for sparse and low-rank unmixing ADSpLRU impose low-rank and sparse constraints on the abundances [16]. However, due to the variability of real scenes, there are differences between the endmembers of an existing spectral library and real scenes, which makes it difficult to accurately describe hyperspectral data and restricts the effectiveness of sparse unmixing algorithms in practical applications.

Another common algorithm is nonnegative matrix factorization (NMF) for unmixing [17]. The matrix decomposition method can obtain an endmember matrix and the corresponding abundance matrix simultaneously, in order to meet the physical meaning of unmixing, abundance values are nonnegative, and this decomposition with the nonnegative constraint can be achieved by the NMF. The objective function of the NMF method is nonconvex, and the constrained regular terms can more effectively reduce the solution space and avoid local optimal solutions [18], [19]. According to row sparseness in abundance matrix, the l_1-norm constraint is used to reinforce sparsity. In addition, since the same endmember is only distributed in

Manuscript received November 6, 2020; revised December 12, 2020; accepted December 28, 2020. Date of publication January 1, 2021; date of current version January 21, 2021. This work was supported in part by the National Natural Science Foundation of China under Grant 41871220 and Grant 41571325, in part by the Fundamental Research Funds for the Central Universities Grant B200202010, and in part by the Natural Science Foundation of Jiangsu Province under Grant BK20181312. *(Corresponding author: Hongjun Su.)*

Pan Zheng and Hongjun Su are with the School of Earth Sciences and Engineering, Hohai University, Nanjing 211100, China (e-mail: zhengpan1013@163.com; hjsu@hhu.edu.cn).

Qian Du is with the Department of Electrical and Computer Engineering, Mississippi State University, Starkville, MS 39762 USA (e-mail: du@ece.msstate.edu).

Digital Object Identifier 10.1109/JSTARS.2020.3048820

individual pixels, its abundances show row and column sparsity, and imposing l_2-norm constraint to the abundance matrix can reinforce the sparsity property [20]–[25]. On the other hand, considering local spatial information, neighborhood regions have similar features and edge areas have different features, distance can be used to measure the relationship between abundances. [26]. Based on this idea, the graph theory is embedded in the NMF model to maintain the local geometric structure, so that high similarity pixels are combined together to improve the performance of unmixing [27]. The graph-based model can only simply express the relationship between two pixels, whereas the hypergraph-based model can represent the higher order relationship between multiple pixels, and the hypergraph model can more accurately express the relationship between spatial and spectral similarity [28]. It can be seen from the preceding NMF-based unmixing algorithms that the prior information used spectral and spatial constraints can improve the unmixing accuracy. However, how to effectively establish the spectral–spatial joint relationship and express data structural information comprehensively and accurately is still a challenging problem.

Under the matrix decomposition framework, spectral and spatial structures are realized through the corresponding constraints, but the complete hyperspectral image structure cannot be transferred. In order to overcome the limitations of NMF and constrained NMF, matrix factorization is extended to tensor factorization. Compared with matrix-based hyperspectral unmixing, tensor factorization is a more natural and structured model. The third-order tensor data structure preserves spatial information without distortion, and is more suitable for hyperspectral data. Zhang *et al*. first introduced nonnegative tensor factorization into the spectral unmixing problem to reduce a hyperspectral image into three factor matrices [29] and the Khatri–Rao product is used to approximate the original tensor image. This approach preserves nonnegativity characteristic of the abundances. However, this method requires prior information on the tensor rank, and it is a nondeterministic polynomial problem. Since then, there have been fewer research works on hyperspectral unmixing algorithms based on tensor factorization. In recent years, some tensor-based unmixing algorithms have appeared. Veganzones *et al*. represent big data hyperspectral time series or multiangle acquisition as tensors, a nonnegative CP decomposition algorithm based on compression is proposed to effectively perform hyperspectral unmixing [30], but the hyperspectral image is still represented by matrix. Tucker decomposition decomposes the tensor into the product of the core tensor and the matrices in each mode since decomposed matrices do not conform to the physical mechanism of unmixing [31]. By combining block term decomposition (BTD), these problems are effectively overcome, and a matrix-vector nonnegative tensor factorization (MV-NTF) unmixing model is established. MV-NTF algorithm decomposes a hyperspectral image into several component tensors, each of which is the outer product of matrix and vector, representing endmember and abundance [32], respectively. Based on this model, Xiong *et al*. introduced the idea of super pixel into MV-NTF, where both global and local information were taken into consideration, avoiding noise interference [33]. Another limitation of the MV-NTF is the lack of constraints that ensure endmembers and abundances are correctly factorized in their respective tensors. Thus, Feng and Wang imposed three constraints on the impervious surface extraction [34]. In summary, there is a certain difference between the process of tensor decomposition and the unmixing process. How to use tensor decomposition to decompose the hyperspectral images and make it conform the physical mechanism of mixed pixels is still an existing problem.

To sum up, sparse unmixing can directly estimate abundances without extracting an endmember matrix, and actual scene features are affected by the environment, which makes true endmembers and those in the spectral library different, thereby affecting unmixing accuracy. NMF unmixing can decompose an image data matrix into endmember and abundance matrices, but spectral and spatial constraints need to be added to compensate for the loss of structural information. Tensor decomposition methods can be used for unmixing without losing the 3-D structure of a hyperspectral image, but the results of some decomposition methods may not have physical significance. Therefore, in the case of maintaining image structure, how to use spatial–spectral characteristics to effectively obtain endmembers and fractional abundances is the focus of this study.

In this article, a sparse and low-rank tensor constrained factorization (SPLRTF) method for hyperspectral unmixing is proposed. Under the framework of MV-NTF unmixing model, considering that each pixel has only a few types of endmembers and inherent data structural information, the proposed method will focus on imposing low-rank and sparse constraints in the estimation process in order to obtain accurate endmember spectra and fractional abundance results.

Compared with other related algorithms, such as ADMM for sparse and low-rank unmixing algorithm (ADSpLRU), ADSpLRU algorithm sets a sliding window, there are few endmembers in the window, the abundance matrix can be sparsely represented. Due to similarity of endmembers in the window, the abundance matrix also has the characteristics of low rank. In this article, two constraints are imposed in the tensor decomposition process, each component tensor decomposed has only one type of endmember, and its corresponding abundance has only a few nonzero values, which is sparse. The endmember only exists in some pixels of the image and also has the characteristics of low rank. The two algorithms have different understandings of sparse and low rank. The contributions of this article are summarized as follows.

1) Regularization for sparsity is incorporated into the MV-NTF framework during the abundance estimation process, making the obtained abundance closer to the true one. This takes advantage of abundance sparsity. Different from ADSpLRU algorithm, this algorithm considering that endmembers in the component tensors obtained by decomposition only account for a small part of all the endmembers, so the abundance is sparse. The results show that this constraint effectively improves the accuracy of hyperspectral unmixing.
2) A low-rank abundance tensor regularization term is introduced in the MV-NTF model, which can be capable of representing the inherent structure of spectra. It is demonstrated from simulated experiments that the imposition

of low-rank constraint on the estimation process helps to improve the unmixing results.

The rest of this article is organized as follows. Notations and preliminaries are briefly introduced in Section II, and Section III introduces the proposed algorithm and optimization method in detail. Section IV uses constructed simulation datasets and three real scene hyperspectral images to illustrate the performance of the proposed algorithm by comparison with commonly used algorithms. Section V discusses the merits of our algorithm. Finally, Section VI concludes this article.

II. Notations and Preliminaries

In this article, scalars are denoted by nonbold italic letters, i.e., x, vectors are denoted by lower case letters, i.e., x, matrices are written in bold capitals letters, i.e., $\mathbf{X}$, and tensors are denoted by calligraphic upper case letters, i.e., $\mathcal{X}$.

A tensor of order *N*, which corresponds to an *N*-dimensional data array, is denoted as $\mathcal{X} \in \mathbb{R}^{I_1 \times \cdots \times I_n \times \cdots \times I_N}$. The elements in an *n*th order tensor are identified by an *n*-tuple of subscripts, i.e., $x_{i_1,i_2,\ldots i_n}$. A scalar is a tensor of order zero, a vector is a first-order tensor, and a matrix is a second-order tensor. Besides, some necessary notations and preliminaries about tensors are introduced as follows.

Definition 1 (Fiber): Fibers are operations that extract vectors from tensors. If one of the dimensions is fixed in a matrix, rows or columns are generated. Similar to matrix operation, the fiber is obtained by fixing other dimensions and retaining only on dimension.

Definition 2 (Slice): Slice is the operation of extracting a matrix from a tensor. If two dimensions are retained in the tensor, the other dimensions are given a matrix, which is a slice of the tensor.

Definition 3 (Mode-n Unfolding): Different from the matrix composed of rows and columns, the *N*-order tensor has *N* modes. Correspondingly, unfolding the tensor in each mode yields a matrix. For example, a third-order tensor $\mathcal{Y} \in \mathbb{R}^{I \times J \times K}$ can be unfolded in three ways, three matrices are defined by

$$\begin{aligned} \left(\mathbf{Y}_{(1)}\right)_{(j-1)K+k,i} &= y_{ijk} \\ \left(\mathbf{Y}_{(2)}\right)_{(k-1)I+i,j} &= y_{ijk} \\ \left(\mathbf{Y}_{(3)}\right)_{(i-1)J+j,k} &= y_{ijk}. \end{aligned} \tag{1}$$

Definition 4 (Inner Product): Given two tensors $\mathcal{X}, \mathcal{Y} \in \mathbb{R}^{I_1 \times I_2 \times \cdots \times I_N}$, their inner product is the sum of the elements of the corresponding elements, i.e.,

$$\langle \mathcal{X}, \mathcal{Y} \rangle = \sum_{i_1=1}^{I_1} \sum_{i_2=1}^{I_2} \cdots \sum_{i_N=1}^{I_N} x_{i_1 i_2 \ldots i_N} y_{i_1 i_2 \ldots i_N}. \tag{2}$$

Definition 5 (Outer Product): Given two tensors $\mathcal{X} \in \mathbb{R}^{I_1 \times I_2 \times \cdots \times I_N}$,$\mathcal{Y} \in \mathbb{R}^{J_1 \times J_2 \times \cdots \times J_M}$, their outer product is a higher order tensor $\mathcal{X} \circ \mathcal{Y} \in \mathbb{R}^{I_1 \times I_2 \times \cdots \times I_N \times J_1 \times J_2 \times \cdots \times J_M}$, and its elements are given by

$$(\mathcal{X} \circ \mathcal{Y})_{i_1 i_2 \ldots i_N j_1 j_2 \ldots j_M} = x_{i_1 i_2 \ldots i_N} y_{j_1 j_2 \ldots j_M}. \tag{3}$$

Definition 6 (Kronecker Product): Kronecker product defines the operation on two matrices $\mathbf{A} \in \mathbb{R}^{I \times J}$ and $\mathbf{B} \in \mathbb{R}^{M \times N}$

$$\mathbf{A} \otimes \mathbf{B} = \begin{bmatrix} \mathrm{a}_{11}\mathbf{B} & \mathrm{a}_{12}\mathbf{B} & \cdots & \mathrm{a}_{1J}\mathbf{B} \\ \mathrm{a}_{21}\mathbf{B} & \mathrm{a}_{22}\mathbf{B} & \cdots & \mathrm{a}_{2J}\mathbf{B} \\ \vdots & \vdots & \ddots & \vdots \\ \mathrm{a}_{I1}\mathbf{B} & \mathrm{a}_{I2}\mathbf{B} & \cdots & \mathrm{a}_{IJ}\mathbf{B} \end{bmatrix} \in \mathbb{R}^{IM \times JN}. \tag{4}$$

Definition 7 (Khatri–Rao Product): Khatri–Rao product defines the operation on two matrices with the same number of columns $\mathbf{A} \in \mathbb{R}^{I \times K}$ and $\mathbf{B} \in \mathbb{R}^{J \times K}$

$$\mathbf{A} \odot \mathbf{B} = \begin{bmatrix} a_1 \otimes b_1 & a_2 \otimes b_2 & \cdots & a_K \otimes b_K \end{bmatrix} \in \mathbb{R}^{IJ \times K}. \tag{5}$$

Let $\mathbf{A} = [\mathbf{A}_1 \ldots \mathbf{A}_N]$ and $\mathbf{B} = [\mathbf{B}_1 \ldots \mathbf{B}_N]$be two block matrices with *N* submatrices, and the partitionwise Khatri–Rao product be defined as

$$\mathbf{A} \overline{\odot} \mathbf{B} = \begin{bmatrix} \mathbf{A}_1 \otimes \mathbf{B}_1 & \mathbf{A}_2 \otimes \mathbf{B}_2 & \cdots & \mathbf{A}_N \otimes \mathbf{B}_N \end{bmatrix}. \tag{6}$$

III. Proposed Method

A. Problem Formulation

Let $\mathbf{Y} \in \mathbb{R}^{L \times M}$denote an *L*-spectral bands hyperspectral image with *M* pixels, and *N* endmembers. A matrix-based unmixing algorithm is to directly decompose an original image matrix into endmember and abundance matrices. The unmixing process can be expressed as

$$\mathbf{Y} = \mathbf{A}\mathbf{X} + \mathbf{E} \tag{7}$$

where $\mathbf{A} \in \mathbb{R}^{L \times N}$ stands for the endmember matrix, $\mathbf{X} \in \mathbb{R}^{N \times M}$ denotes the fractional abundance, and $\mathbf{E} \in \mathbb{R}^{L \times M}$ represents the measurement errors. The linear mixing model is commonly used to solve (7). Qian *et al*. proposed an MV-NTF model that combines BTD and Tucker decomposition [32], and it has been proved to be effective in hyperspectral unmixing. This approach decomposes the 3-D hyperspectral image into the sum of *N* component tensors, each component is the outer product of a matrix and vector, representing abundance and endmember, respectively. It can be formulated as

$$\mathcal{X} = \sum_{n=1}^{N} \mathcal{X}_n + \mathcal{E} = \sum_{n=1}^{N} \mathbf{E}_n \circ \mathbf{C}_n + \mathcal{E} = \sum_{n=1}^{N} \mathbf{A}_n \mathbf{B}_n^T \circ \mathbf{C}_n + \mathcal{E} \tag{8}$$

where $\mathcal{X} \in \mathbb{R}^{I \times J \times K}$ denotes the 3-D hyperspectral image with $I \times J$ pixels and *K* bands, and $\mathcal{X}_n$ is the *n*th component tensor. $\mathbf{E}_n \in \mathbb{R}^{I \times J}$represents the abundance map of the *n*th endmember made up of two matrices $\mathbf{A}_n \in \mathbb{R}^{I \times NL}$ and $\mathbf{B}_n \in \mathbb{R}^{J \times NL}$, *L* is the rank of abundance maps, $\mathbf{C}_n$ is the *n*th endmember, and $\mathcal{E}$ denotes the error item.

Unmixing with the MV-NTF model is to decompose a 3-D hyperspectral image into the sum of several component tensors, and each component tensor is the outer product of abundance and endmember matrices. For each component tensor, it contains only one endmember. When it is decomposed into the outer product of two matrices, each abundance matrix contains only a small number of nonzero values, which is characterized by sparseness. This sparsity can be used to achieve better results, so the sparsity constraint is imposed in the decomposition process.

The rank of the matrix or the tensor can represent the inherent spectral characteristics. Thus, low-rank representation uses rank as sparse measure. For each component tensor, there is only one endmember. Most of the pixels in this tensor are similar. The component tensor contains less information and its rank is low. According to this spatial feature information, using a kernel norm to perform low-rank constraints can obtain more effective unmixing accuracy. Each component tensor is the outer product of an endmember and its abundance, so the abundance correlation and spectral correlation are high. Each abundance tensor is constrained by low rank, which can better represent the characteristics of each corresponding endmember. The regularization parameter is used to flexibly change the low-rank constraint on estimated abundance, which can fully express the fine structure and details beyond the low-rank structure [35].

Combining the aforementioned two characteristics, a new tensor decomposition unmixing algorithm is proposed.

B. Proposed Model

For each hyperspectral image χ , MV-NTF model can be used to decompose it into the sum of several tensor components, the process can be expressed by the following formula:

$$\min_{\chi} \left\| \chi - \sum_{n=1}^{N} \chi_n \right\|_F^2 \tag{9}$$

where $\chi \in \mathbb{R}^{I\times J\times K}$ denotes the hyperspectral image and N is the number of tensor components, which is equal to the number of endmembers. According to the decomposition principle of the MV-NTF model, each tensor component can be decomposed into the outer product of two matrices, three-mode unfolding of the hyperspectral image is used for matrix representation

$$\mathbf{X}_{IJ\times K} = \left[(\mathbf{A}_1 \odot \mathbf{B}_1)\, 1\mathbf{L}_1 \cdots (\mathbf{A}_N \odot \mathbf{B}_N)\, 1\mathbf{L}_N\right] \cdot \mathbf{C}^T \tag{10}$$

$$\mathbf{X}_{JK\times I} = (\mathbf{B} \overline{\odot} \mathbf{C}) \cdot \mathbf{A}^T \tag{11}$$

$$\mathbf{X}_{KI\times J} = (\mathbf{C} \overline{\odot} \mathbf{A}) \cdot \mathbf{B}^T. \tag{12}$$

The . operator requires that the matrix involved in the operation must be of the same dimension. The operation rule of the . operator is to multiply each corresponding element one by one. The objective function (9) becomes

$$\min_{\mathbf{A},\mathbf{B},\mathbf{C}} \left\| \chi - \sum_{n=1}^{N} \mathbf{A}_n {\mathbf{B}_n}^T \circ \mathrm{c}_n \right\|_F^2 \tag{13}$$

where c_n is the nth endmember vector and $\mathbf{A}_n {\mathbf{B}_n}^T$ is the corresponding abundance matrix. As previously stated, using the intrinsic structural characteristics is helpful to improve the unmixing accuracy. Based on the discussion in Section III-A, by imposing the low-rankness and sparsity property on the abundance map, the sparse and low-rank tensor decomposition (SPLRTF) model is introduced as

$$\min_{\mathbf{A},\mathbf{B},\mathbf{C}} \left\| \chi - \sum_{n=1}^{N} \mathbf{A}_n {\mathbf{B}_n}^T \circ \mathrm{c}_n \right\|_F^2 + \lambda \sum_{n=1}^{N} \left\| \mathbf{A}_n {\mathbf{B}_n}^T \right\|_0 + \tau \sum_{n=1}^{N} \mathrm{rank}(\mathbf{A}_n {\mathbf{B}_n}^T) \tag{14}$$

where $\lambda, \tau \geq 0$ are parameters that control the tradeoff between the sparsity and rank regularization terms. The first term makes the obtained endmembers and abundance matrices as close to the original image as possible. The l_0-norm is an NP-hard problem, which is difficult to solve, and estimating the rank of matrix is also an unsolved problem. In order to solve formula (14), the formula is rewritten as

$$\min_{\mathbf{A},\mathbf{B},\mathbf{C}} \left\| \chi - \sum_{n=1}^{N} \mathbf{A}_n {\mathbf{B}_n}^T \circ \mathrm{c}_n \right\|_F^2 + \lambda \sum_{n=1}^{N} \left\| \mathbf{A}_n {\mathbf{B}_n}^T \right\|_1 + \tau \sum_{n=1}^{N} \left\| \mathbf{A}_n {\mathbf{B}_n}^T \right\|_*. \tag{15}$$

Using convex relaxation methods, the sparsity and low-rankness constraint terms are replaced with l_1-norm and nuclear norm, respectively. Being parameterized, (15) becomes flexible enough to impose either one of the two constraints on abundance. For example, by setting $\lambda = 0$, the low-rank constraint is only imposed to the abundance map, which is named LRTF algorithm, whereas setting $\tau = 0$ is tantamount to impose the sparsity property, and reduced to SPTF algorithm.

The proposed model provides an advantage over either low-rank or sparse estimation methods, which will be demonstrated in Section IV.

C. Optimization Procedure

We use one of the common convex optimization tools to solve this function, which is an ADMM-based technique. The optimization problem can be divided into several subproblems, each of which is solved by a different method during iteration. In the iterative process, when solving one of the variables, other variables need to be fixed.

By introducing some auxiliary variables for $\mathbf{A}$ and $\mathbf{B}$, the original problem is reformulated into its ADMM form

$$\begin{aligned} &\min_{\mathbf{U}_1,\mathbf{V}_1,\mathbf{U}_2,\mathbf{V}_2} \left\| \chi - \sum_{n=1}^{N} \mathbf{A}_n {\mathbf{B}_n}^T \circ \mathrm{c}_n \right\|_F^2 \\ &\quad + \lambda \left\| \mathbf{U}_1 {\mathbf{V}_1}^T \right\|_1 + \tau \left\| \mathbf{U}_2 {\mathbf{V}_2}^T \right\|_* \\ &\text{s.t } \mathbf{U}_1 - \mathbf{A} = 0, \mathbf{V}_1 - \mathbf{B} = 0, \mathbf{U}_2 - \mathbf{A} = 0, \mathbf{V}_2 - \mathbf{B} = 0. \end{aligned} \tag{16}$$

Introducing auxiliary variables $\mathbf{U}_1, \mathbf{V}_2, \mathbf{U}_1$, and $\mathbf{V}_2$, the augmented Lagrangian form of formula (16) is

$$\begin{aligned} L = &\min_{\mathbf{A}_n,\mathbf{B}_n,\mathbf{C}_n,\mathbf{U}_1,\mathbf{V}_1,\mathbf{U}_2,\mathbf{V}_2} \frac{1}{2} \left\| \chi - \sum_{n=1}^{N} \mathbf{A}_n {\mathbf{B}_n}^T \circ \mathrm{c}_n \right\|_F^2 \\ &+ \lambda \left\| \mathbf{U}_1 {\mathbf{V}_1}^T \right\|_1 \\ &+ \tau \left\| \mathbf{U}_2 {\mathbf{V}_2}^T \right\|_* + tr\left[\mathbf{D}_1^T (\mathbf{U}_1 - \mathbf{A})\right] + tr\left[\mathbf{D}_2^T (\mathbf{U}_2 - \mathbf{A})\right] \\ &+ tr\left[\mathbf{D}_3^T (\mathbf{V}_1 - \mathbf{B})\right] + tr\left[\mathbf{D}_4^T (\mathbf{V}_2 - \mathbf{B})\right] \\ &+ \frac{\mu}{2} \left(\|\mathbf{A} - \mathbf{U}_1\|_F^2 + \|\mathbf{B} - \mathbf{V}_1\|_F^2 \right. \\ &\left. + \|\mathbf{A} - \mathbf{U}_2\|_F^2 + \|\mathbf{B} - \mathbf{V}_2\|_F^2 \right) \end{aligned} \tag{17}$$

where $\mathbf{D}_1, \mathbf{D}_2, \mathbf{D}_3$, and $\mathbf{D}_4$are the Lagrange multipliers, and $\mu>0$ is a positive penalty parameter and its controls the balance between the original and auxiliary variables.

Let $\mathbf{U} = [\mathbf{U}_1\ \mathbf{U}_2]^T$ and $\mathbf{V} = [\mathbf{V}_1\ \mathbf{V}_2]^T$, then (17) can be written in an equivalent form as

$$L = \min_{\mathbf{A}_n,\mathbf{B}_n,\mathbf{C}_n,\mathbf{U}_1,\mathbf{V}_1,\mathbf{U}_2,\mathbf{V}_2} \frac{1}{2}\left\|\chi - \sum_{n=1}^{N}\mathbf{A}_n{\mathbf{B}_n}^T \circ \mathrm{c}_n\right\|_F^2 + \lambda\left\|\mathbf{U}_1{\mathbf{V}_1}^T\right\|_1 + \tau\left\|\mathbf{U}_2{\mathbf{V}_2}^T\right\|_* + \frac{\mu}{2}\left(\|\mathbf{A}-\mathbf{U}-\mathbf{\Lambda}\|_F^2 + \|\mathbf{B}-\mathbf{V}-\mathbf{\Lambda}\|_F^2\right) \tag{18}$$

where $\mathbf{\Lambda} = [\mathbf{\Lambda}_1^T\ \mathbf{\Lambda}_2^T\ \mathbf{\Lambda}_3^T\ \mathbf{\Lambda}_4^T]^T$,$\mathbf{\Lambda}_i = (1/\mu)\mathbf{D}_i, i = 1,\ldots,4$, contains the scaled Lagrange multipliers.

Fix other variables, solve the Lagrangian function for only one of them, and update the variables separately in the same way.

Update A: In the iterative process of solving $\mathbf{A}$, a Mode-I unfolding of the hyperspectral image tensor is used for calculation. Removing the unrelated items of $\mathbf{A}$, the subproblem for $\mathbf{A}$ becomes

$$f(\mathbf{A}) = \min_{\mathbf{A}} \frac{1}{2}\left\|\mathbf{X}_{JK\times I} - (\mathbf{B}\overline{\odot}\mathbf{C})\cdot\mathbf{A}^T\right\|_F^2 + \frac{\mu}{2}\left(\|\mathbf{A}-\mathbf{U}-\mathbf{\Lambda}\|_F^2\right). \tag{19}$$

Taking the partial derivative with respect to $\mathbf{A}$, the update rule for $\mathbf{A}$ is obtained

$$\mathbf{A} \leftarrow \mathbf{A}.*(\chi^T\mathbf{S} + \mu(\mathbf{U}_1 + \mathbf{\Lambda}_1 + \mathbf{U}_2 + \mathbf{\Lambda}_2))./\mathbf{A}(\mathbf{S}^T\mathbf{S} + 2\mu\mathbf{I}) \tag{20}$$

$$\mathbf{S} = \mathbf{B}\circ\mathbf{C}. \tag{21}$$

Update B: Unfolding the image tensor into matrix of Mode-II, the subproblem of optimization for $\mathbf{B}$ is similar to $\mathbf{A}$

$$f(\mathbf{B}) = \min_{\mathbf{B}} \frac{1}{2}\left\|\mathbf{X}_{KI\times J} - (\mathbf{C}\overline{\odot}\mathbf{A})\cdot\mathbf{B}^T\right\|_F^2 + \frac{\mu}{2}\left(\|\mathbf{B}-\mathbf{V}-\mathbf{\Lambda}\|_F^2\right). \tag{22}$$

Taking the partial derivative with respect to $\mathbf{B}$, the update rule for $\mathbf{B}$ is obtained

$$\mathbf{B} \leftarrow \mathbf{B}.*(\chi^T\mathbf{S} + \mu(\mathbf{V}_1 + \mathbf{\Lambda}_3 + \mathbf{V}_2 + \mathbf{\Lambda}_4))./\mathbf{B}(\mathbf{S}^T\mathbf{S} + 2\mu\mathbf{I}) \tag{23}$$

$$\mathbf{S} = \mathbf{A}\circ\mathbf{C}. \tag{24}$$

Update C: Unfolding the image tensor into matrix of Mode-III, and extracting all the items related to $\mathbf{C}$, the subproblem of optimization for $\mathbf{C}$ is written as

$$f(\mathbf{C}) = \min_{\mathbf{C}} \|\mathbf{X}_{IJ\times K} - [(\mathbf{A}_1\odot\mathbf{B}_1)\,1\mathbf{L}_1 \cdots (\mathbf{A}_N\odot\mathbf{B}_N)\,1\mathbf{L}_N]\cdot\mathbf{C}^T\|_F^2. \tag{25}$$

Taking the partial derivative of $\mathbf{C}$, the update rule for $\mathbf{C}$ is

$$\mathbf{C} \leftarrow \mathbf{C}.*\chi^T\mathbf{S}./(\mathbf{C}\mathbf{S}^T\mathbf{S}) \tag{26}$$

$$\mathbf{S} = [(\mathbf{A}_1\odot\mathbf{B}_1)\,1_L \cdots (\mathbf{A}_R\odot\mathbf{B}_R)\,1_L]. \tag{27}$$

Algorithm 1: The Proposed SPLRTF Algorithm.

Inputs: A hyperspectral imageχ Select parameters λ, τ
Initialize **A, B, C, U, V**
Repeat
$\mathbf{A} \leftarrow$
$\mathbf{A}.*(\chi^T\mathbf{S} + \mu(\mathbf{U}_1 + \mathbf{\Lambda}_1 + \mathbf{U}_2 + \mathbf{\Lambda}_2))./\mathbf{A}(\mathbf{S}^T\mathbf{S} + 2\mu\mathbf{I})$
$\mathbf{B} \leftarrow$
$\mathbf{B}.*(\chi^T\mathbf{S} + \mu(\mathbf{V}_1 + \mathbf{\Lambda}_1 + \mathbf{V}_2 + \mathbf{\Lambda}_2))./\mathbf{B}(\mathbf{S}^T\mathbf{S} + 2\mu\mathbf{I})$
$\mathbf{C} \leftarrow \mathbf{C}.*\chi^T\mathbf{S}./(\mathbf{C}\mathbf{S}^T\mathbf{S})$
$\mathbf{U}_1 = SHR(\lambda\|\mathbf{U}_1{\mathbf{V}_1}^T\|_1 + \frac{\mu}{2}\|\mathbf{A}-\mathbf{U}_1-\mathbf{\Lambda}_1\|_F^2)$
$\mathbf{V}_1 = \mathrm{SHR}(\lambda\|\mathbf{U}_1{\mathbf{V}_1}^T\|_1 + \frac{\mu}{2}\|\mathbf{B}-\mathbf{V}_1-\mathbf{\Lambda}_1\|_F^2)$
$\mathbf{U}_2 = SVT(\tau\|\mathbf{U}_2{\mathbf{V}_2}^T\|_* + \frac{\mu}{2}\|\mathbf{A}-\mathbf{U}_2-\mathbf{\Lambda}_2\|_F^2)$
$\mathbf{V}_2 = \mathrm{SVT}(\tau\|\mathbf{U}_2{\mathbf{V}_2}^T\|_* + \frac{\mu}{2}\|\mathbf{B}-\mathbf{V}_2-\mathbf{\Lambda}_2\|_F^2)$
$\mathbf{\Lambda}_1 = \mathbf{\Lambda}_1 - \mathbf{A}+\mathbf{U}_1$
$\mathbf{\Lambda}_2 = \mathbf{\Lambda}_1 - \mathbf{A}+\mathbf{U}_2$
$\mathbf{\Lambda}_3 = \mathbf{\Lambda}_3 - \mathbf{B}+\mathbf{V}_1$
$\mathbf{\Lambda}_4 = \mathbf{\Lambda}_3 - \mathbf{B}+\mathbf{V}_2$
Until convergence
Output: Abundance tensor $\mathbf{A}\mathbf{B}^T$ and endmember matrix $\mathbf{C}$

Update $\mathbf{U}_1$ *and* $\mathbf{V}_1$: The subproblems of $\mathbf{U}_1$ and $\mathbf{V}_1$ are similar. The subproblems of $\mathbf{U}_1$ and $\mathbf{V}_1$ are

$$f(\mathbf{U}_1) = \arg\min \lambda\left\|\mathbf{U}_1{\mathbf{V}_1}^T\right\|_1 + \frac{\mu}{2}\|\mathbf{A}-\mathbf{U}_1-\mathbf{\Lambda}_1\|_F^2 \tag{28}$$

$$f(\mathbf{V}_1) = \arg\min \lambda\left\|\mathbf{U}_1{\mathbf{V}_1}^T\right\|_1 + \frac{\mu}{2}\|\mathbf{B}-\mathbf{V}_1-\mathbf{\Lambda}_1\|_F^2. \tag{29}$$

The iterative shrinkage thresholding algorithm can be used to solve these subproblems.

Update $\mathbf{U}_2$ *and* $\mathbf{V}_2$ The subproblems of $\mathbf{U}_2$: and $\mathbf{V}_2$ are also similar. The subproblems of $\mathbf{U}_2$ and $\mathbf{V}_2$ are

$$f(\mathbf{U}_2) = \arg\min \tau\left\|\mathbf{U}_2{\mathbf{V}_2}^T\right\|_* + \frac{\mu}{2}\|\mathbf{A}-\mathbf{U}_2-\mathbf{\Lambda}_2\|_F^2 \tag{30}$$

$$f(\mathbf{V}_2) = \arg\min \tau\left\|\mathbf{U}_2{\mathbf{V}_2}^T\right\|_* + \frac{\mu}{2}\|\mathbf{B}-\mathbf{V}_2-\mathbf{\Lambda}_2\|_F^2. \tag{31}$$

The singular value thresholding method can be used to solve these subproblems.

Update$\mathbf{\Lambda}$: The scaled Lagrange multipliers update rules are

$$\mathbf{\Lambda}_1 = \mathbf{\Lambda}_1 - \mathbf{A}+\mathbf{U}_1 \tag{32}$$

$$\mathbf{\Lambda}_2 = \mathbf{\Lambda}_1 - \mathbf{A}+\mathbf{U}_2 \tag{33}$$

$$\mathbf{\Lambda}_3 = \mathbf{\Lambda}_3 - \mathbf{B}+\mathbf{V}_1 \tag{34}$$

$$\mathbf{\Lambda}_4 = \mathbf{\Lambda}_3 - \mathbf{B}+\mathbf{V}_2. \tag{35}$$

The iteration stop criterion setting is similar to MV-NTF. There are two stopping criteria for optimization in our algorithms. When the number of iterations is greater than 3000, or the change of the objective function is less than 1e-4, the optimization process will stop. In the simulation data experiment, the initial endmember matrix $\mathbf{C}$ and abundance matrix $\mathbf{A}\mathbf{B}^T$ are known. For real data, the initial endmember matrix $\mathbf{C}$

and abundance matrix $\mathbf{AB}^T$ are obtained by VCA [36] or FCLS [37] algorithms, and $\mathbf{A}$ and $\mathbf{B}$ are obtained by the NMF-based decomposition of abundance matrix $\mathbf{AB}^T$.

The proposed algorithm, referred to as the SPLRTF unmixing algorithm, is summarized in Algorithm 1.

IV. Experiments

Both simulated and real image data experiments were conducted to validate the performance of the proposed SPLRTF.

We implemented seven related hyperspectral unmixing methods for comparison, i.e., the popular sparse unmixing algorithm SUnSAL, simultaneously sparse and low-rank unmixing method ADSpLRU, MV-NTF algorithm, subspace structure regularized NMF algorithm (in experiments, this algorithm is abbreviated as Zhou's method)[38], kurtosis-based smooth NMF algorithm KbSNMF[39], and also compare it with only sparse or low-rank constraint algorithms SPTF and LRTF to prove the ability of these two constraints in tensors.

Spectral angle distance (SAD) is used to evaluate the dissimilarity of *n*th real endmember signature c_n and its estimated signature $\widehat{c_n}$, which is defined as

$$\mathrm{SAD}_n = \arccos\left(\frac{c_n^T \widehat{c_n}}{\|c_n\| \, \|\widehat{c_n}\|}\right). \tag{36}$$

The root-mean-square error (RMSE) measures the error between *n*th abundance map $\mathbf{E}_n$ and *n*th estimated abundance$\widehat{\mathbf{E}_n}$ [40], which is defined as

$$\mathrm{RMSE}_n = \sqrt{\frac{1}{M}\left\|\mathbf{E}_n - \widehat{\mathbf{E}_n}\right\|_2^2} \tag{37}$$

where M is the total pixel number of the image, $\mathbf{E}_n$ denotes *n*th ground truth abundance, and $\widehat{\mathbf{E}_n}$ is the *n*th estimated abundance.

Signal-to-reconstruction error (SRE) is used to evaluate the unmixing accuracy between original image $\mathbf{X}$ and mixed image $\widehat{\mathbf{X}}$, which is defined as

$$\mathrm{SRE} = 10\log_{10}\frac{E\left[\|\mathbf{X}\|_2^2\right]}{E\left[\left\|\mathbf{X}-\widehat{\mathbf{X}}\right\|_2^2\right]}. \tag{38}$$

A. Simulated Data Experiments

Nine pure signatures are selected from the USGS library to generate endmembers, which contain 224 bands, covering wavelengths ranging from 0.38 to 2.5 μm. The abundance matrix is generated according to actual needs, satisfying the sum to one and nonnegative constraints. The abundance maps are constructed using the method in [41]. The LMM model can be used to obtain 3-D simulated hyperspectral images. To simulate different types of hyperspectral image data, three different cases are constructed to test the performance of proposed method. The details are listed as follows.

Case 1: In order to test the robustness of the proposed algorithm, different degrees of Gaussian noise are added to the clean image cube. For simplicity, considering SNR levels of 20, 25, 30, 35, 40, 45, 50 dB, the simulated image data have different noise levels.

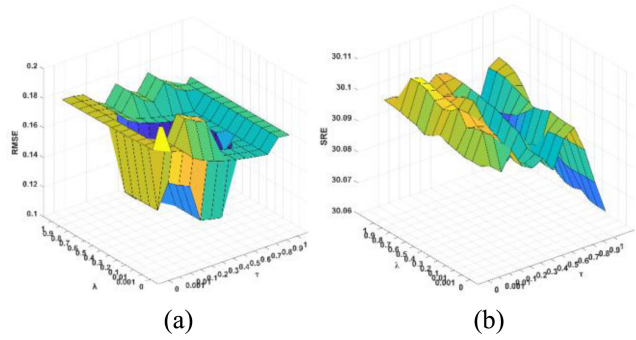

Fig. 1. Performance of SPLRTF when λ and τtake values from 0.001 to 1. (a) RMSE. (b) SRE.

Case 2: Different images have different number of spectral signatures in the real scenes. In order to verify the applicability of the proposed algorithm to different scenes effectively, hyperspectral images are generated by selecting 3, 6, or 9 endmembers from the USGS library.

Case 3: Different pixel numbers of images show different spectral, spatial, and spectral–spatial structure, so five kinds of pixel number cubes are constructed to evaluate the unmixing algorithm performance.

Parameter Setting: In the proposed SPLRTF algorithm, two constraints were imposed on the abundance map, and there are two regularization parameters and one Lagrange parameter. The purpose of this analysis is to find a better parameter range for the convenience of subsequent simulation data experiments. After obtaining the initialization data, using the case of SNR = 25 dB, first fix one of the parameters $\mu = 0.1$, both regularization parameters were changed from 0, 1e-3, 1e-2, 0.1, 0.2, 0.3, 0.4, 0.5, 0.6, 0.7, 0.8, 0.9 to 1. The influence of different SNR of the proposed algorithm will be discussed in Section IV. The proposed SPLRTF algorithm was tested using different values of λ and τ. Fig. 1(a) shows the RMSE results of algorithm when the regularization parameters change, and Fig. 1(b) shows the SRE results. The smaller the RMSE, the larger the SRE, the better the effect of the unmixing.

The parameter λ shows the sparse constraint on unmixing performance, and τ shows the low-rank constraint on unmixing performance. From the figures, SRE results as a whole show a decreasing trend with the increase of λ and the decrease of τ, and when τ equals 0.01 and λ equals 0.9, the SRE is the largest. It can be discovered that RMSE results are the smallest when λ is in the range of 0.4 to 0.7 and τ is in the range of 0.4 to 0.6. When λ is 0, which is equivalent to removing the sparse term, the proposed algorithm becomes SPTF; when τ equals 0, it is equivalent to removing the low-rank term, and the algorithm becomes LRTF. In subsequent experiments, we will also add these two algorithms to the comparative experiments. When $\lambda = 0$ and $\tau = 0$, the proposed SPLRTF method is simplified into MV-NTF model, and the RMSE and SAD change trends show that these two constraints have significant effects. In order to get better results, we set λ to 0.4 and τ to 0.7 in the following simulated data experiments.

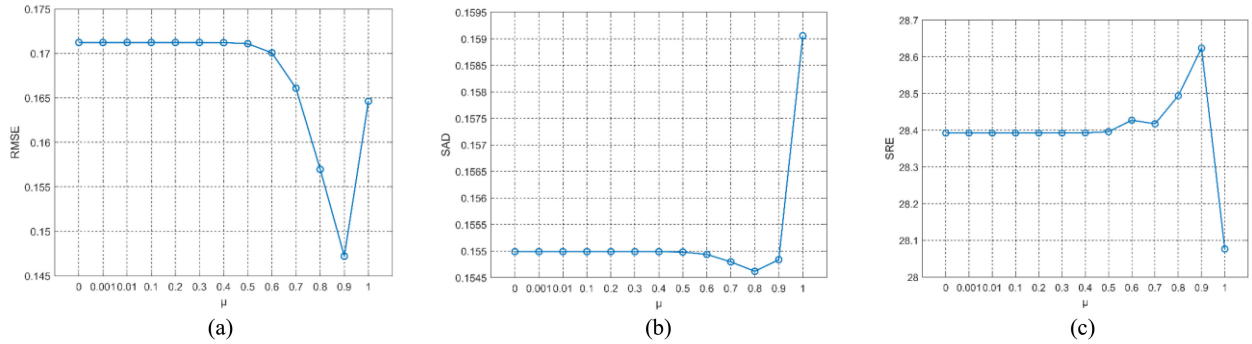

Fig. 2. Performance of SPLRTF obtained by different values of μ. (a) RMSE. (b) SAD. (c) SRE.

TABLE I
RMSE, SAD, AND SRE RESULTS OF COMPARISON ALGORITHMS ON SIMULATED DATA

	SUnSAL	ADSpLRU	MV-NTF	SPTF	LRTF	KbSNMF	Zhou's Method	SPLRTF
RMSE	0.3829	0.2328	0.1624	0.1496	0.1493	0.2287	0.2679	**0.1336**
SAD	-	-	0.1680	0.1578	0.1564	0.4574	0.6230	**0.1550**
SRE	25.6408	25.6412	20.2819	25.9630	25.9670	26.7900	25.1551	**26.9587**

According to the aforementioned experiments, using the case of SNR = 25 dB, fixing $\lambda = 0.7$ and $\tau = 0.4$, and μ being changed from 0, 1e-3, 1e-2, 0.1, 0.2, 0.3, 0.4, 0.5, 0.6, 0.7, 0.8, 0.9 to 1, Fig. 2(a) illustrates the RMSE result changes, Fig. 2(b) shows the SAD changes, and Fig. 2(c) shows the change trend of SRE results. When μ is 0.9, both RMSE and SAD reach the minimum value, and SRE is the maximum. Therefore, we set μ to 0.9 in the following simulation experiments.

Experiment with the parameters set above compares the proposed algorithm with other seven algorithms. Since SUnSAL and ADSpLRU algorithms can obtain abundance matrices without endmember matrices, only the SRE and RMSE results are compared. It can be seen from Table I that the RMSE value of the SPLRTF algorithm is much lower than other comparison algorithms, that is, the estimated abundance maps obtained by unmixing are closest to the real data and the SRE result is larger than the others, which means the proposed algorithm has the best accuracy. The SAD result of SPLRTF algorithm is the lowest among comparison algorithms, indicating that the obtained endmembers are the most similar to the real endmembers.

After comparing these seven algorithms with the proposed algorithm in this article using simulated hyperspectral data, it can be found that the unmixing performance of the SPLRTF algorithm is better than MV-NTF, SUnSAL, ADSpLRU, KbSNMF, Zhou's method, SPTF, and LRTF algorithms.

B. Real-Data Experiments

Jasper, Samson, and Chang'E-3 VNIS datasets were used for real-data experiments. These real scene datasets were collected by different sensors, with different endmembers and different sizes, which can verify the applicability of the proposed algorithm. The parameter settings of the comparison experiments refer to the original article. The parameters of SPLRTF algorithm use grid search method to select the best parameters. Three indicators are used to evaluate the performance. ADSpLRU and SUnSAL algorithms can obtain the abundance matrices directly from the spectral library without calculating the endmember matrices, therefore, only RMSE results can be calculated for these two algorithms.

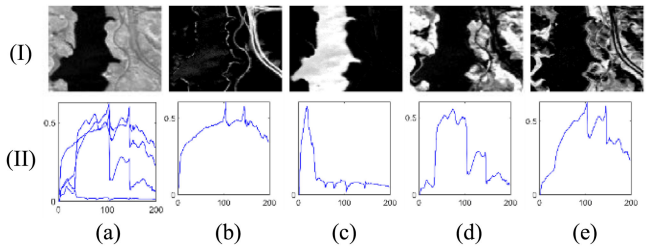

Fig. 3. (I-a) 58th band image of Jasper data. (II-a) Four ground truth endmembers of Jasper data. (b) Abundance map and endmember spectral of road. (c) Abundance map and endmember spectral of water. (d) Abundance map and endmember spectral of tree. (e) Abundance map and endmember spectral of soil.

1) Jasper Ridge Data: Jasper Ridge data have been widely used in performance testing of hyperspectral image unmixing. Jasper hyperspectral image data were collected on Jasper Ridge Natural Reserve in California, USA. Jasper Ridge contains 512 × 614 pixels, 224 bands ranging from 380 to 2500 nm recorded, and the spectral resolution is 9.46 nm. After removing 1–3, 108–112, 154–166, and 220–224 bands, there are 188 bands. The 58th band image of the subimage of Jasper Ridge data is shown in Fig. 3(I-a), which is composed of 100 × 100 pixels. There are four endmembers in this subimage: tree, soil, water, and road, the ground truth endmembers and abundance maps are shown in Fig. 3(b)–(e) [42].

The endmembers obtained by SPLRTF are given in Fig. 4, from which ground truth endmembers and estimated endmembers can be seen intuitively. The SAD results of SPLRTF and comparison algorithms are shown in Table II , the best results of each algorithm are bolded. In general, the SAD value of SPLRTF is the smallest, which means that the endmember accuracy is

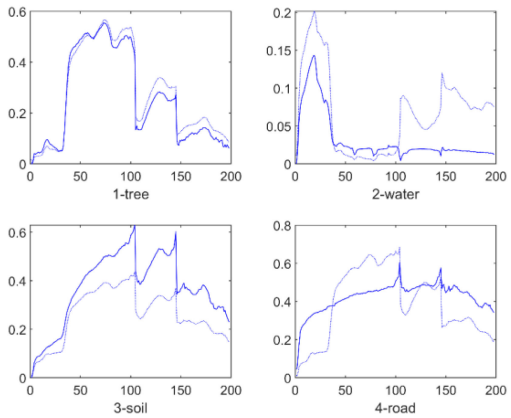

Fig. 4. Four endmembers obtained by SPLRTF on Jasper Data. Solid lines represent the ground truth endmembers and dotted lines represent estimated endmembers.

TABLE II
SAD RESULTS OF COMPARISON ALGORITHMS ON JASPER DATA

	MV-NTF	SPTF	LRTF	KbSNMF	Zhou's Method	SPLRTF
tree	0.2324	**0.0861**	0.0902	0.1242	0.1881	0.1990
water	0.3435	0.4478	0.4728	**0.1220**	0.3261	0.3269
soil	0.3354	0.1133	**0.1060**	1.2505	0.2076	0.2082
road	0.3382	0.3528	0.3396	0.9331	0.2865	**0.2450**
Avg	0.3124	0.2500	0.2522	0.6075	0.2521	**0.2448**

TABLE III
SRE RESULTS OF COMPARISON ALGORITHMS ON JASPER DATA

ALGORITHMS	SRE
MV-NTF	30.7522
SPTF	35.3070
LRTF	34.3692
KbSNMF	20.9673
Zhou's Method	14.6407
SPLRTF	**42.2367**

the highest. For the endmembers, adding sparse or low-rank constrains can yield better results than the original MV-NTF algorithm. As shown in Table III, the SRE is greater than other algorithms, which demonstrates the imposed sparse and low-rank constraints on the tensor decomposition can improve unmixing performance. The RMSE results of the proposed method is smaller than the original tensor decomposition method MV-NTF and average RMSE of four abundances of the SPLRTF algorithm is small than other comparison algorithms as shown in Table IV. The abundance maps are given in Fig. 5.

2) Samson Data: Samson hyperspectral image is obtained by Florida Environment Research Institute using Samson sensor. These data contain 156 bands from 401 to 889 nm, and its spectral resolution is 3.13 nm. The original image size is 952×952 pixels, in order to reduce the experimental time, a subimage with 100×100 pixels is used for unmixing. This subimage contains three types of features: soil, water, and trees. Fig. 6(I-a) shows a band image of Samson data. Besides, the ground truth endmembers and the corresponding abundance maps are shown in Fig. 6(b)–(d) [42].

The differences between endmembers obtained by SPLRTF and ground truth endmembers are shown in Fig. 7. The SAD results are given in Table V, from which it can be seen that the average value obtained by SPLRTF has better results. Table VI shows that the SPLRTF algorithm has a higher SRE value than the MV-NTF algorithm, which means that the unmixing result of SPLRTF algorithm is better. Table VII shows that compared with SUnSAL, ADSpLRU, MV-NTF, Zhou's method, and KbSNMF algorithms, the proposed algorithm still performs the best, and both SPTF algorithm and LRTF algorithm yield higher accuracy than the original MV-NTF algorithm, reflecting the sparse and low-rank constraints play an important role in unmixing. Fig. 8 shows the abundance maps of Samson data obtained by four algorithms and the results of each algorithm can be seen from the figures clearly.

3) Chang'E-3 VNIS Data: The hyperspectral scene under experiment is a portion of the young lava plain of northern Imbrium by the VNIS sensor over lunar surface. In the real-data experiments, visible and near-infrared channel with a spectral range of 450 to 950 nm are used. In this spectral range, the main minerals of the lunar surface can be effectively identified.

All VNIS hyperspectral images acquired by Chang'E-3 are marked on Fig. 9 [43], including the images of the four points CD5, CD6, CD7, and CD8 with the size of 256×256 and the band number of 100. The spatial resolution is about 0.5 mm and the spectral interval is 5 nm. In order to unmix the hyperspectral images, the level 2B VNIS data in PDS format were first reduced by bad line, bad points, and flat field corrections, and were then converted into reflectance values [44]. In the experiments, without any prior information, HFC was adopted to estimate the number of endmembers, and VCA was used to initialize data.

The estimated endmembers of four images are shown in Fig. 10. For Chang'E-3 VNIS datasets, the ground truth endmembers and abundances are unknown, and the SRE results can only be calculated to compare the unmixing performance of different algorithms on these data. The SRE comparison is shown in Table VIII, where the SRE results of the SPLRTF method for different images are the largest. Either the algorithm with only sparse constraint SPTF or only low-rank constraint LRTF is larger than the SRE results of MV-NTF, indicating that these two constraints are effective for hyperspectral unmixing. The abundance maps obtained by four images are shown in Fig. 11. The colorbar indicates the proportion of each endmember, and the abundance of each endmember can be clearly seen.

Using these three hyperspectral images from different sensors to conduct experiments, it can be seen from the SRE results and RMSE results that the proposed algorithm performs better on these three data than other comparison algorithms, which shows the effectiveness of the proposed algorithm to a certain extent. The abundance maps obtained by the proposed algorithm SPLRTF using three hyperspectral images can clearly reflect the distribution and proportion of each endmember.

V. DISCUSSIONS

The novelty of the proposed algorithm is to apply sparse and low-rank constraints to the abundance estimation process

TABLE IV
RMSE RESULTS OF COMPARISON ALGORITHMS ON JASPER RIDGE DATA

	SUnSAL	ADSpLRU	MV-NTF	SPTF	LRTF	KbSNMF	Zhou's Method	SPLRTF
tree	**0.1697**	0.1703	0.3867	0.3951	0.3950	0.2048	0.6191	0.2557
water	0.4689	0.4670	0.2976	0.2999	0.2998	0.2798	0.5350	**0.2156**
soil	0.5680	0.5668	0.3957	**0.2039**	0.2048	0.2097	0.3827	0.2042
road	0.3495	**0.3471**	0.5704	0.5604	0.5605	0.5606	0.4917	0.5598
Avg	0.3890	0.3878	0.4126	0.3648	0.3650	0.3137	0.5071	**0.3088**

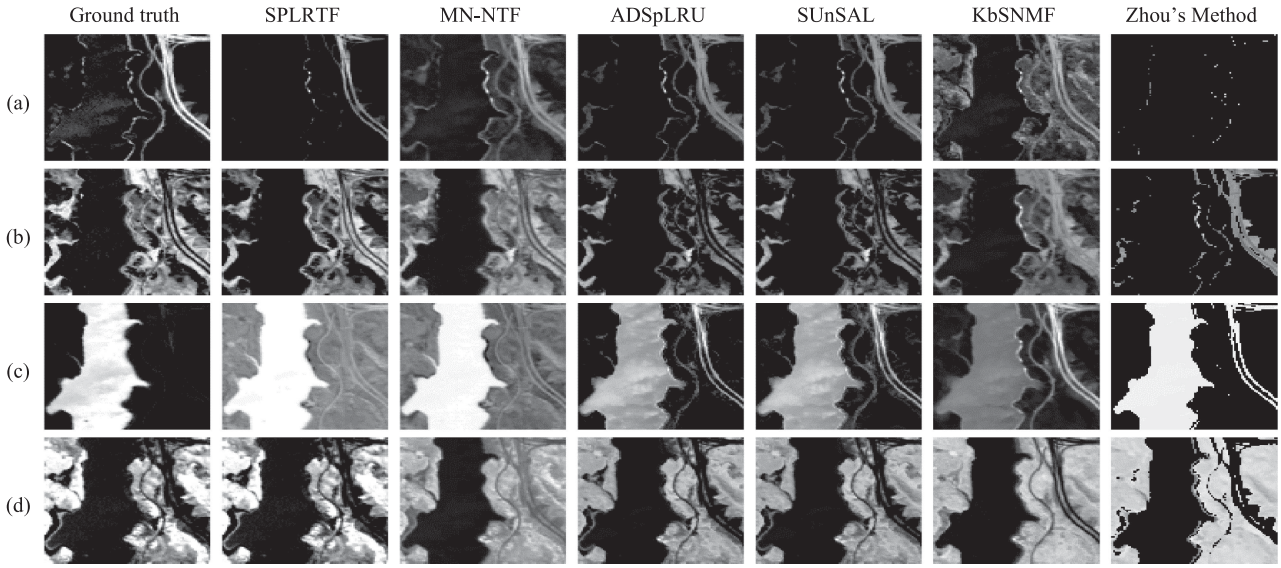

Fig. 5. Abundance maps obtained by comparison algorithms on Jasper Ridge data. From left to right, the columns are the abundance maps of ground truth, SPLRTF, MV-NTF, ADSpLRU, SUnSAL, KbSNMF, and Zhou's method. (a) Road. (b) Soil. (c) Water. (d) Tree.

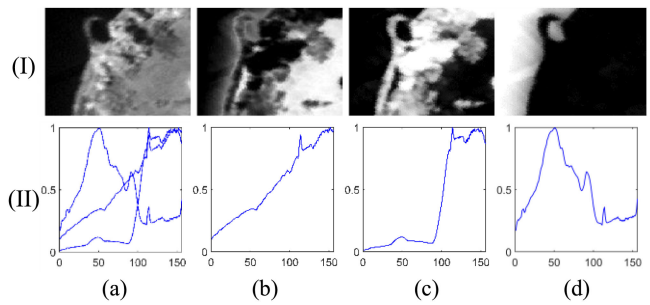

Fig. 6. (I-a) 156th band image of Samson data. (II-a) Three ground truth endmembers of Samson data. (b) Abundance map and endmember spectral of soil. (c) Abundance map and the endmember spectral of tree. (d) Abundance map and the endmember spectral of water.

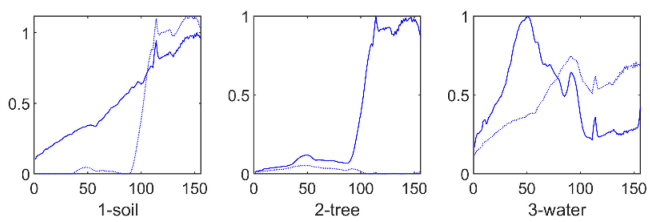

Fig. 7. Three endmembers obtained by SPLRTF on Samson Data. Solid lines represent the ground truth endmembers and dotted lines represent estimated endmembers.

TABLE V
SAD RESULTS OF COMPARISON ALGORITHMS ON SAMSON DATA

	MV-NTF	SPTF	LRTF	KbSNMF	Zhou's Method	SPLRTF
Soil	**0.2543**	0.3131	0.3128	0.4138	0.453	0.2805
Tree	0.7543	**0.7027**	0.7028	1.5546	0.683	0.7054
Water	0.0911	0.0364	0.0373	0.4569	0.2682	**0.0330**
Avg	0.3666	0.3507	0.3510	0.8084	0.4681	**0.3396**

TABLE VI
SRE RESULTS OF COMPARISON ALGORITHMS ON SAMSON DATA

ALGORITHMS	SRE
KbSNMF	19.1001
Zhou's Method	18.3924
MV-NTF	18.2373
SPTF	17.6764
LRTF	18.2179
SPLRTF	**19.2423**

in tensor decomposition. These constraints are more in line with the pixel mixing mechanism, and simulation and real data experiments verify its effectiveness. This section further analyzes the influence of these improvements on unmixing effect through further experiments, and verify the stability from the perspective of different image sizes and noise resistance.

TABLE VII
RMSE RESULTS OF COMPARISON ALGORITHMS ON SAMSON DATA

	SUnSAL	ADSpLRU	MV-NTF	SPTF	LRTF	KbSNMF	Zhou's Method	SPLRTF
Water	0.5161	0.4430	0.5034	0.4660	0.4673	0.4593	0.5762	**0.4256**
Soil	0.5475	0.4149	0.4412	0.4661	0.4618	0.5615	0.6123	**0.3738**
Tree	**0.2743**	0.4700	0.4380	0.4145	0.4184	0.3928	0.5770	0.4447
Avg	0.4460	0.4426	0.4609	0.4489	0.4492	0.4712	0.5885	**0.4147**

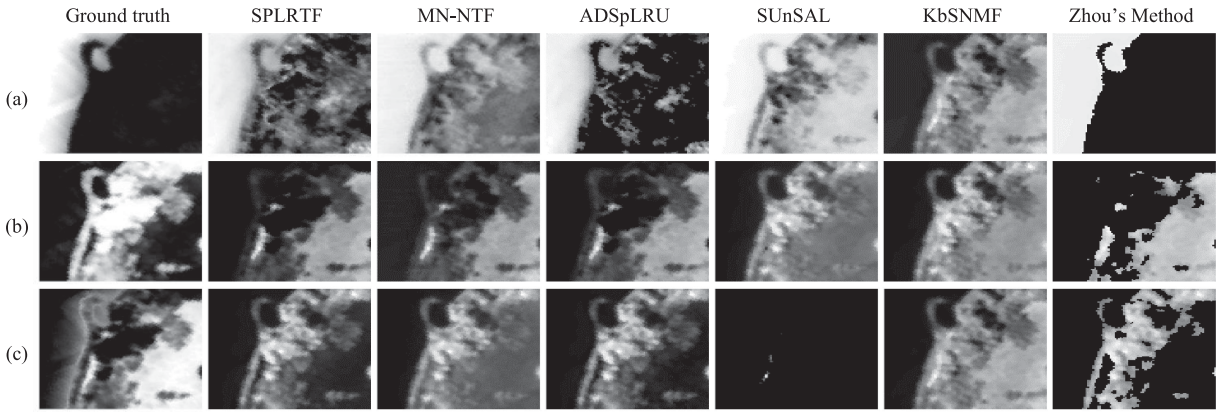

Fig. 8. Abundance maps obtained by comparison algorithms on Samson data. From left to right, the columns are the abundance maps of ground truth, SPLRTF, MV-NTF, ADSpLRU, SUnSAL, KbSNMF, and Zhou's method. (a) Water. (b) Tree. (c) Soil.

TABLE VIII
SRE RESULTS OF COMPARISON ALGORITHMS ON CHANG'E-3 VNIS DATA

	SUnSAL	ADSpLRU	MV-NTF	SPTF	LRTF	KbSNMF	Zhou's Method	SPLRTF
CD5	10.7595	23.5644	17.4561	21.3491	19.9304	22.2363	18.2245	**23.6348**
CD6	10.8610	25.0104	13.7741	19.4805	20.2904	23.6718	21.4983	**25.8222**
CD7	11.5892	8.5560	6.3673	14.4203	13.7392	12.6203	15.9084	**19.1746**
CD8	10.2012	13.4813	7.8844	13.3940	17.3108	17.9416	14.3859	**22.2445**

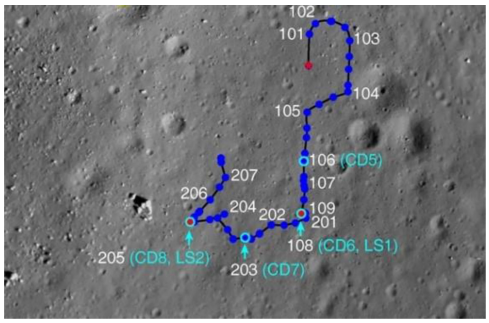

Fig. 9. Map of the path traversed by the Yutu rover and the distribution of detection points [43].

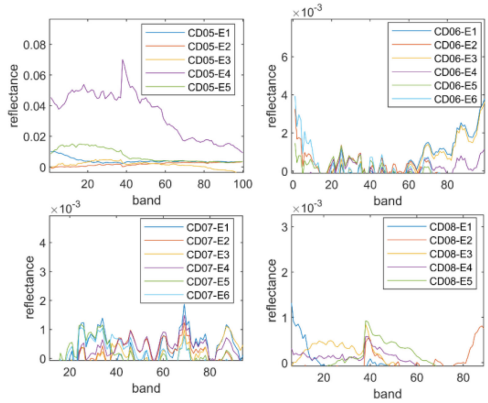

Fig. 10. Estimated endmembers of four VNIS images.

A. *Effectiveness of the Sparse and Low-Rank Constraints*

In this article, sparse and low-rank constraints are imposed on the tensor factorization process for unmixing, and two parameters are used to control the tradeoff between the sparsity and rank regularization terms. The SPTF algorithm and LRTF algorithm have higher accuracy than MV-NTF algorithm in both simulated and real data experiments, which means that the imposed constraints can improve the precision of hyperspectral unmixing. By comparing SPLRTF algorithm with MV-NTF, SPTF, and LRTF algorithms, it can be seen that SPLRTF achieves better unmixing performance revealing the effective role of the two constraints in unmixing.

B. *Comparison of Algorithms Under Different Noises*

Compared the proposed SPLRTF method with MV-NTF, SUnSAL, SPTF, LRTF, KbSNMF, and Zhou's method under

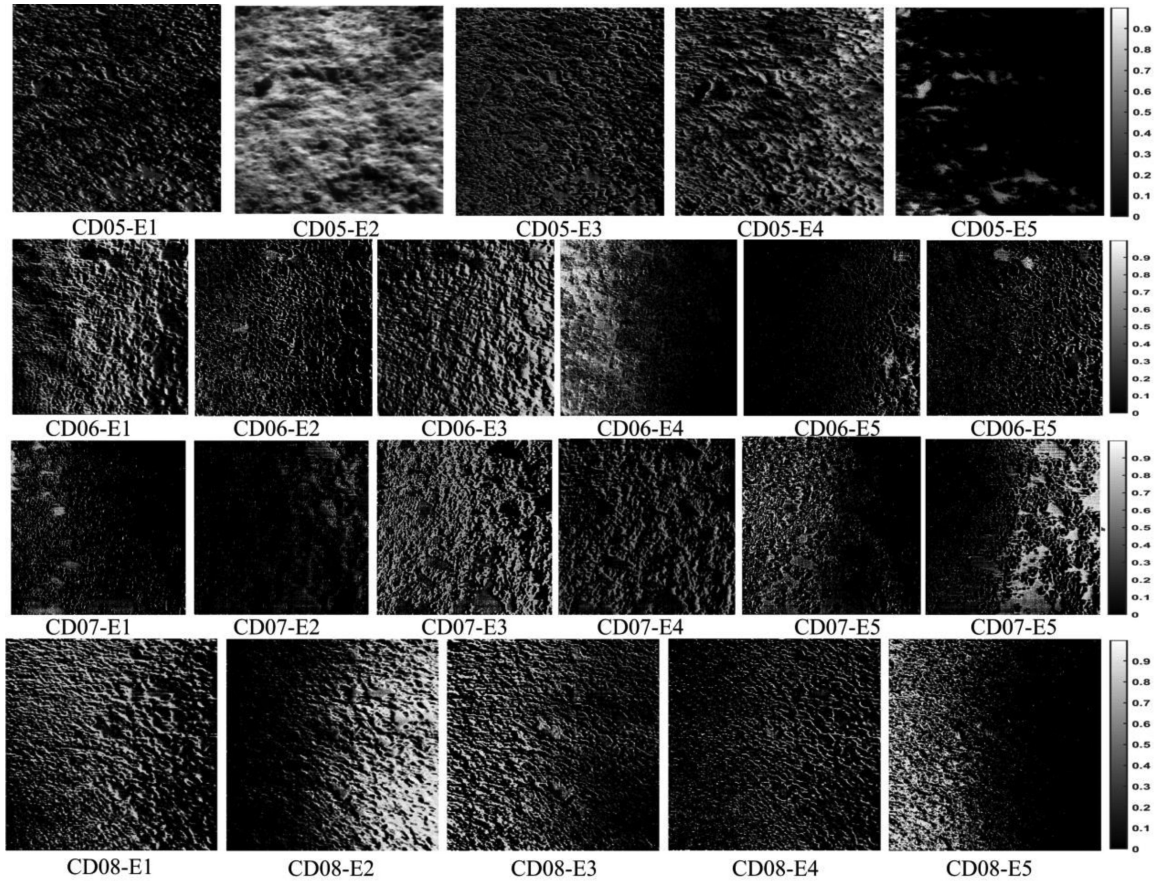

Fig. 11. Abundance maps of four VNIS images. From top to bottom, the rows are CD5 abundance maps, CD6 abundance maps, CD7 abundance maps, and CD8 abundance maps.

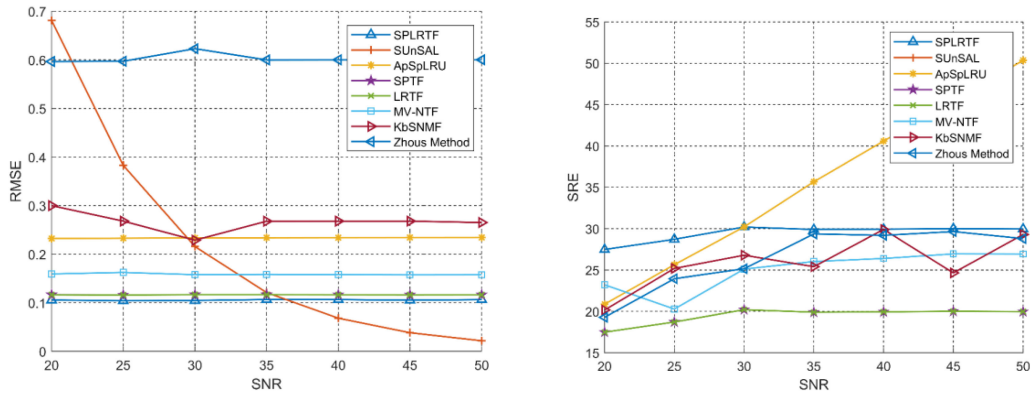

Fig. 12. Performance of SPLRTF obtained by different noise levels. (a) RMSE. (b) SRE.

different noise levels, Fig. 12 shows that as the SNR changes, the RMSE results and SAD results of MV-NTF, SUnSAL, SPTF, LRTF, and KbSNMF algorithms are stable and robust. The proposed SPLRTF method has lower RMSE results and higher SRE results than other comparison algorithms. At high noise levels, the RMSE of the SUnSAL method is the smallest and the SRE is the largest, but it is sensitive to noise and the results are unstable.

C. Comparison of Algorithms in Different Pixel Numbers

This experiment aims to reveal the structural performance of the proposed SPLRTF algorithm through simulated data of different sizes. Small sizes of the simulated cube may have less information, whereas large images have rich spatial, spectral, and spatial–spectral information. From Fig. 13, it can be observed that the RMSE results become smaller and the SRE

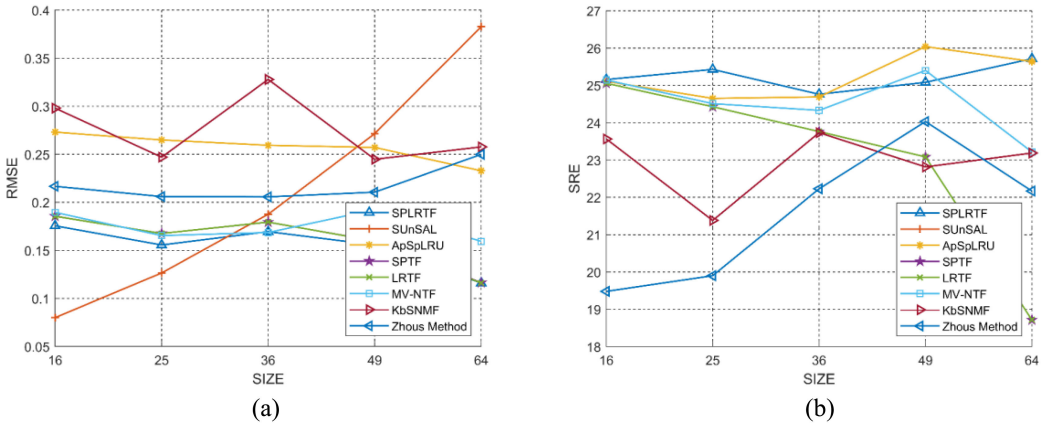

Fig. 13. Performance of SPLRTF obtained by different pixel numbers. (a) RMSE. (b) SRE.

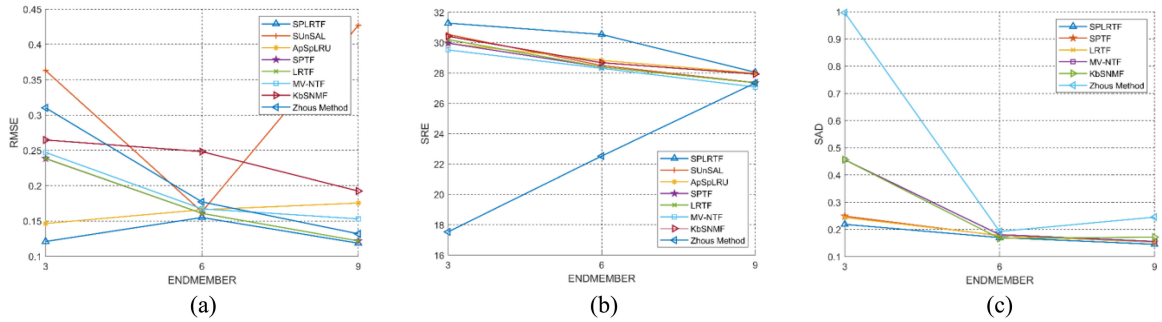

Fig. 14. Performance of SPLRTF obtained by different endmember numbers. (a) RMSE. (b) SRE. (c) SAD.

TABLE IX
COMPUTING TIME OF COMPARISON ALGORITHMS (IN SECONDS)

	JASPER	SAMSON	CE'3-CD5	CE'3-CD6	CE'3-CD7	CE'3-CD8
SUnSAL	0.1833	0.1594	0.4971	0.2088	0.1904	0.5091
ADSpLRU	34.9073	20.5741	47.4124	33.2052	34.2071	39.2149
MV-NTF	1648.6198	585.3913	373.8058	829.7708	1674.4646	455.1919
SPTF	12.4799	11.7937	12.5651	15.6694	11.6128	6.9516
LRTF	12.3063	11.7781	39.9510	38.8358	35.7314	35.8551
KbSNMF	45.0491	32.9209	136.1522	138.3268	45.0135	52.8486
Zhou's Method	36.2516	24.8967	518..9997	184.7529	177.903	138.5935
SPLRTF	12.3933	11.8382	40.0353	35.4135	33.3785	33.4148

results become larger as the image size increases. The RMSE of the proposed SPLRTF as a whole is lower than other algorithms and its SRE is higher than other algorithms. Comparing the matrix-based methods SUnSAL, ADSpLRU, KbSNMF, and Zhou's method with other tensor-based algorithms, it can be found that the results of the tensor-based algorithms are better than the matrix-based methods, indicating that loss of spatial structure degrades the unmixing accuracy.

D. Comparison of Algorithms in Different Endmember Numbers

In this experiment, unmixing accuracy is evaluated with respect to endmember number changes. Fig. 14(a) and (b) present the RMSE and SRE values of the SPLRT method and seven comparison algorithms, which show that the SPLRTF algorithms perform well with different endmember numbers. Fig. 14(c) shows the SAD results of six algorithms, because the ADSpLRU and SUnSAL algorithms can only obtain abundance matrices. Fig. 14(c) shows that the algorithms perform better in the case of more endmembers than in the case of fewer endmembers, but on the whole, SPLRTF algorithm has a higher unmixing accuracy than MV-NTF.

E. Computing Time

As shown in Table IX, the proposed method SPLRTF with the ADMM-based optimization has a faster convergence rate

than MV-NTF, and SPLRTF algorithm has a shorter running time than MV-NTF. SPTF method takes less time than LRTF algorithm because LRTF performs singular value decomposition, which takes a long time. Comparing the running time of the matrix-based ADSpLRU with the tensor-based algorithm, it can be found that their calculation speeds are similar.

VI. Conclusion

In this article, a new tensor factorization method SPLRTF was proposed for hyperspectral unmixing. Based on the original matrix-vector tensor factorization unmixing method, the proposed algorithm abandons the original low-rank constraint that specifies the rank of pixels, but chooses a more flexible low-rank constraint in the abundance estimation process. Considering the distribution of ground features, sparsity is considered as an inherent property of abundances, and the sparse constraint is added to ensure the accuracy of endmember and abundance maps. The simulated data and three real scene hyperspectral image experiments are carried out to validate the proposed SPLRTF. The accuracy index and the displayed abundance maps show that the proposed algorithm can offer better unmixing results.

References

[1] P. Ghamisi *et al.*, "Advances in hyperspectral image and signal processing: A comprehensive overview of the state-of-the-art," *IEEE Geosci. Remote Sens. Mag.*, vol. 5, no. 4, pp. 37–78, Dec. 2017.

[2] J. M. Bioucas-Dias *et al.*, "Hyperspectral unmixing overview: Geometrical, statistical, and sparse regression-based approaches," *IEEE J. Sel. Topics Appl. Earth Observ. Remote Sens.*, vol. 5, no. 2, pp. 354–379, Apr. 2012.

[3] J. W. Boardman, F. A. Kruse, and R. O. Green, "Mapping target signatures via partial unmixing of AVIRIS data," in *Proc. Summaries JPL Airborne Earth Sci. Workshop*, pp. 23–26, 1995.

[4] M.-D. Iordache, J. M. Bioucas-Dias, and A. Plaza, "Sparse unmixing of hyperspectral data," *IEEE Trans. Geosci. Remote Sens.*, vol. 49, no. 6, pp. 2014–2039, Jun. 2011.

[5] P. Du *et al.*, "Advances of four machine learning methods for spatial data handling: A review," *J. Geovis. Spatial Anal.*, vol. 4, no. 1, pp. 1–25, May 2020.

[6] H. Su, Y. Yu, Z. Wu, and Q. Du, "Random subspace-based k-nearest class collaborative representation for hyperspectral image classification," *IEEE Trans. Geosci. Remote Sens.*, to be published, doi: 10.1109/TGRS.2020.3029578.

[7] H. Su, Y. Yu, Q. Du, and P. Du, "Ensemble learning for hyperspectral image classification using tangent collaborative representation," *IEEE Trans. Geosci. Remote Sens.*, vol. 58, no. 6, pp. 3778–3790, Jun. 2020.

[8] H. Su, B. Zhao, Q. Du, P. Du, and Z. Xue, "Multifeature dictionary learning for collaborative representation classification of hyperspectral imagery," *IEEE Trans. Geosci. Remote Sens.*, vol. 56, no. 4, pp. 2467–2484, Apr. 2018.

[9] H. Su, W. Yao, Z. Wu, P. Zheng, and Q. Du, "Kernel low-rank representation with elastic net for China coastal wetland land cover classification using GF-5 hyperspectral imagery," *ISPRS J. Photogrammetry Remote Sens.*, vol. 171, pp. 238–252, Jan. 2021.

[10] J. M. Rodríguez Alves, J. M. P. Nascimento, J. M. Bioucas-Dias, A. Plaza, and V. Silva, "Parallel sparse unmixing of hyperspectral data," in *Proc. Int. Geosci. Remote Sens. Symp.*, 2013, vol. 49, no. 6, pp. 1446–1449.

[11] M. Iordache, J. M. Bioucas-Dias, and A. Plaza, "Total variation spatial regularization for sparse hyperspectral unmixing," *IEEE Trans. Geosci. Remote Sens.*, vol. 50, no. 11, pp. 4484–4502, Nov. 2012.

[12] J. M. Bioucas-Dias and M. A. T. Figueiredo, "Alternating direction algorithms for constrained sparse regression: Application to hyperspectral unmixing," in *Proc. 2nd Workshop Hyperspectral Image Signal Process., Evol. Remote Sens.*, 2010, pp. 1–4.

[13] M.-D. Iordache, J. M. Bioucas-Dias, and A. Plaza, "Collaborative sparse unmixing of hyperspectral data," in *Proc. IEEE Int. Geosci. Remote Sens. Symp.*, Munich, Germany, Jul. 2012, pp. 7488–7491.

[14] R. Wang, H.-C. Li, and Z.-K. Yin, "Collaborative sparse unmixing of hyperspectral data considering the difference of endmembers," *Dianzi Keji Daxue Xuebao/J. Univ. Electron. Sci. Technol. China*, vol. 43, no. 6, pp. 813–816 and 828, Nov. 2014.

[15] H. Su, B. Zhao, Q. Du, and P. Du, "Kernel collaborative representation with local correlation features for hyperspectral image classification," *IEEE Trans. Geosci. Remote Sens.*, vol. 57, no. 2, pp. 1230–1241, Feb. 2019.

[16] P. V. Giampouras, K. E. Themelis, A. A. Rontogiannis, and K. D. Koutroumbas, "Simultaneously sparse and low-rank abundance matrix estimation for hyperspectral image unmixing," *IEEE Trans. Geosci. Remote Sens.*, vol. 54, no. 8, pp. 4775–4789, Aug. 2016.

[17] L. Miao and H. Qi, "Endmember extraction from highly mixed data using minimum volume constrained nonnegative matrix factorization," *IEEE Trans. Geosci. Remote Sens.*, vol. 45, no. 3, pp. 765–777, Mar. 2007.

[18] X. Geng, L. Ji, and K. Sun, "Non-negative matrix factorization based unmixing for principal component transformed hyperspectral data," *Frontiers Inf. Technol. Electron. Eng.*, vol. 17, no. 5, pp. 403–412, May 2016.

[19] J. Peng, Y. Zhou, W. Sun, Q. Du, and L. Xia, "Self-paced nonnegative matrix factorization for hyperspectral unmixing," *IEEE Trans. Geosci. Remote Sens.*, to be published, doi: 10.1109/TGRS.2020.3016941.

[20] B. Du, L. Zhang, D. Tao, N. Wang, and T. Chen, "A spectral dissimilarity constrained nonnegative matrix factorization based cancer screening algorithm from hyperspectral fluorescence images," in *Proc. Int. Conf. Comput. Healthcare*, Hong Kong, Dec. 2012, pp. 112–119.

[21] W. Y. Lee and M. Andrews, "Blind spectral unmixing for compressive hyperspectral imaging of highly mixed data," in *Proc. IEEE Int. Conf. Image Process.*, 2014, pp. 1312–1316.

[22] P. Thouvenin, N. Dobigeon, and J. Tourneret, "Hyperspectral unmixing with spectral variability using a perturbed linear mixing model," *IEEE Trans. Signal Process.*, vol. 64, no. 2, pp. 525–538, Jan. 2016.

[23] Y. Qian, S. Jia, J. Zhou, and A. Robles-Kelly, "Hyperspectral unmixing via $L_{1/2}$ sparsity-constrained nonnegative matrix factorization," *IEEE Trans. Geosci. Remote Sens.*, vol. 49, no. 11, pp. 4287–4297, Nov. 2011.

[24] X. Li, J. Zhou, L. Tong, X. Yu, J. Guo, and C. Zhao, "Structured discriminative nonnegative matrix factorization for hyperspectral unmixing," in *Proc. IEEE Int. Conf. Image Process.*, 2016, pp. 1848–1852.

[25] J. Sigurdsson, M. O. Ulfarsson, and J. R. Sveinsson, "Hyperspectral unmixing with l_q regularization," *IEEE Trans. Geosci. Remote Sens.*, vol. 52, no. 11, pp. 6793–6806, Nov. 2014.

[26] W. He, H. Zhang, and L. Zhang, "Hyperspectral unmixing using total variation regularized reweighted sparse non-negative matrix factorization," in *Proc. IEEE Int. Geosci. Remote Sens. Symp.*, 2008, pp. 7034–7037.

[27] X. Lu, H. Wu, Y. Yuan, P. Yan, and X. Li, "Manifold regularized sparse NMF for hyperspectral unmixing," *IEEE Trans. Geosci. Remote Sens.*, vol. 51, no. 5, pp. 2815–2826, May 2013.

[28] W. Wang, Y. Qian, and Y. Y. Tang, "Hypergraph-regularized sparse NMF for hyperspectral unmixing," *IEEE J. Sel. Topics Appl. Earth Observ. Remote Sens.*, vol. 9, no. 2, pp. 681–694, Feb. 2016.

[29] Q. Zhang, H. Wang, R. Plemmons, and V. P. Pauca, "Spectral unmixing using nonnegative tensor factorization," in *Proc. ACM 45th Annu. Southeast Regional Conf.*, 2007, pp. 531–532.

[30] M. A. Veganzones, J. E. Cohen, R. Cabral Farias, J. Chanussot, and P. Comon, "Nonnegative tensor CP decomposition of hyperspectral data," *IEEE Trans. Geosci. Remote Sens.*, vol. 54, no. 5, pp. 2577–2588, May 2016.

[31] G. Favier and A. L. F. de Almeida, "Overview of constrained PARAFAC models," *EURASIP J. Adv. Signal Process.*, vol. 2014, no. 1, pp. 1–25, Sep. 2014.

[32] Y. Qian, F. Xiong, S. Zeng, J. Zhou, and Y. Y. Tang, "Matrix-vector nonnegative tensor factorization for blind unmixing of hyperspectral imagery," *IEEE Trans. Geosci. Remote Sens.*, vol. 55, no. 3, pp. 1776–1792, Mar. 2017.

[33] F. Xiong, J. Chen, J. Zhou, and Y. Qian, "Superpixel-based nonnegative tensor factorization for hyperspectral unmixing," in *Proc. IEEE Int. Geosci. Remote Sens. Symp.*, Valencia, Spain, Jul. 2018, pp. 6392–6395.

[34] B. Feng and J. Wang, "Constrained nonnegative tensor factorization for spectral unmixing of hyperspectral images: A case study of urban impervious surface extraction," *IEEE Geosci. Remote Sens. Lett.*, vol. 16, no. 4, pp. 583–587, Apr. 2019.

[35] T. Imbiriba, R. A. Borsoi, and J. C. M. Bermudez, "Low-rank tensor modeling for hyperspectral unmixing accounting for spectral variability," *IEEE Trans. Geosci. Remote Sens.*, vol. 58, no. 3, pp. 1833–1842, Mar. 2020.

[36] J. M. P. Nascimento and J. M. B. Dias, "Vertex component analysis: A fast algorithm to unmix hyperspectral data" *IEEE Trans. Geosci. Remote Sens.*, vol. 43, no. 4, pp. 898–910, Apr. 2005.

[37] D. C. Heinz and C.-I. Chang, "Fully constrained least squares linear spectral mixture analysis method for material quantification in hyperspectral imagery," *IEEE Trans. Geosci. Remote Sens.*, vol. 39, no. 3, pp. 529–545, Mar. 2001.
[38] L. Zhou *et al.*, "Subspace structure regularized nonnegative matrix factorization for hyperspectral unmixing," *IEEE J. Sel. Topics Appl. Earth Observ. Remote Sens.*, vol. 13, pp. 4257–4270, Jul. 2020.
[39] E. M. M. B. Ekanayake *et al.*, "Constrained nonnegative matrix factorization for blind hyperspectral unmixing incorporating endmember independence," Apr. 2020. [Online]. Available: https://arxiv.org/abs/2003.01041
[40] R. Guerra, L. Santos, S. López, and R. Sarmiento, "A new fast algorithm for linearly unmixing hyperspectral images," *IEEE Trans. Geosci. Remote Sens.*, vol. 53, no. 12, pp. 6752–6765, Dec. 2015.
[41] M.-D. Iordache, "A sparse regression approach to hyperspectral unmixing," Ph.D. dissertation, Univ. Técnica de Lisboa, Dept. Elect. Comput. Eng., Lisbon, Portugal, Nov. 2011.
[42] F. Zhu, "Hyperspectral unmixing: Ground truth labeling datasets benchmark performances and survey," Aug. 2017. [Online] Available: https://arxiv.org/abs/1708.05125
[43] B. Liu *et al.*, "Reflectance conversion methods for the VIS/NIR imaging spectrometer aboard the chang'E-3 lunar rover: Based on ground validation experiment data," *Res. Astron. Astrophys.*, vol. 13, no. 7, pp. 862–874, Jul. 2013.
[44] B. Liu *et al.*, "Data processing and preliminary results of the chang'E-3 VIS/NIR imaging spectrometer in-situ analysis," *Res. Astron. Astrophys.*, vol. 14, no. 12, pp. 1578–1594, Nov. 2014.

Pan Zheng received the B.E. degree in surveying and mapping engineering, in 2018 from the School of Earth Sciences and Engineering, Hohai University, Nanjing, China, where she is currently working toward the M.E. degree in photogrammetry and remote sensing.

Her research interests include hyperspectral remote sensing imagery, collaborative representation, and machine learning in hyperspectral unmixing.

Hongjun Su (Senior Member, IEEE) received the Ph.D. degree in cartography and geography information system from the Key Laboratory of Virtual Geographic Environment (Ministry of Education), Nanjing Normal University, Nanjing, China, in 2011.

He is currently a Full Professor with the School of Earth Sciences and Engineering, Hohai University, Nanjing, China. His main research interests include hyperspectral remote sensing dimensionality reduction, classification, and spectral unmixing.

Dr. Su is an Associate Editor for the IEEE JOURNAL OF SELECTED TOPICS IN APPLIED EARTH OBSERVATIONS AND REMOTE SENSING. He was the recipient of the 2016 Best Reviewer Award from the IEEE Geoscience and Remote Sensing Society.

Qian Du (Fellow, IEEE) received the Ph.D. degree in electrical engineering from the University of Maryland, Baltimore, MD, USA, in 2000.

She is currently the Bobby Shackouls Professor with the Department of Electrical and Computer Engineering, Mississippi State University, Starkville, MS, USA. Her research interests include hyperspectral image analysis and applications, pattern classification, data compression, and neural networks.

Dr. Du is a Fellow of the SPIE—International Society for Optics and Photonics. She was a Co-Chair of the Data Fusion Technical Committee of the IEEE Geoscience and Remote Sensing Society from 2009 to 2013, and the Chair of the Remote Sensing and Mapping Technical Committee of the International Association for Pattern Recognition from 2010 to 2014. She has served as an Associate Editor for the IEEE JOURNAL OF SELECTED TOPICS IN APPLIED EARTH OBSERVATIONS AND REMOTE SENSING, the *Journal of Applied Remote Sensing*, and the *IEEE Signal Processing Letters*. From 2016 to 2020, she was the Editor-in-Chief for the IEEE JOURNAL OF SELECTED TOPICS IN APPLIED EARTH OBSERVATIONS AND REMOTE SENSING. She currently is a member of IEEE Periodicals Review and Advisory Committee.